Postseismic Relaxation Along the San Andreas Fault at Parkfield from Continuous Seismological Observations

F. Brenguier, *et al.*

Science **321**, 1478 (2008);
DOI: 10.1126/science.1160943

Science (print ISSN 0036-8075; online ISSN 1095-9203) is published weekly, except the last week in December, by the American Association for the Advancement of Science, 1200 New York Avenue NW, Washington, DC 20005.

tion. A minimum value of 1.25 nT was measured a few seconds before CA and below the ionospheric peak around 17:42 and 17:50 (altitudes of 1270 and 1200 km, respectively).

Between approximately 1200 and 1600 km altitude (points I and II), the draped magnetic field was antiparallel to the corotation direction (the toward lobe). Because Cassini was at northern latitudes, this lobe corresponds to the draping of a field that was initially southward. However, the IMF surrounding Titan was clearly northward, and there is no possibility that such an orientation could lead to a toward lobe at northern latitudes. A comparison between the average field in Titan's magnetotail during T32 with that in the toward lobe during three north latitude flybys with almost identical geometries (T28, T29, and T30) inside Saturn's magnetosphere shows that these directions differed by as little as 28°. The fields in the toward lobes of flybys T32 and T30 (Fig. 3) display high similarity (8° between averages).

In the absence of an internal field, the fields just above Titan's collisional ionosphere are draped kronian magnetospheric fields deposited within Titan's induced magnetosphere before the moon's magnetosheath excursion. These fields are effectively frozen or "fossilized" in the near-Titan noncollisional plasma as a result of mass loading by cold ions [notably N_2^+ (*19*)] from Titan's exosphere below 1600 km, dramatically reducing the transit speed of magnetic flux tubes. As Titan entered the magnetosheath, it encountered shocked solar wind traveling along the Sun-Saturn direction. This flow transported IMF field lines, which piled up and draped around the layers of fossilized fields, as shown by the monotonic change in the magnetic field strength after 17:53. Thus, draped field lines at higher altitudes moved at higher speeds, reflecting more recently sampled magnetic environments.

The detection of kronian fossil fields during T32 occurred because their convection time was longer than the time that Titan was exposed to the IMF. In the early hours of day 164, Titan was immersed in the magnetosheath longer than Cassini (9 hours, 45 min), because the spacecraft was inside Titan's orbit. For the same reason, Titan was within Saturn's magnetosphere for a shorter time than the interval from B to C. However, this was long enough to replenish Titan's induced magnetosphere with kronian fields after the first magnetosheath excursion. Hence, if Titan was within Saturn's magnetosphere for some time between B and C, and if the replenishment time was the same for the IMF and magnetospheric fields, the time spent by Titan in Saturn's magnetosphere between B and C should have been longer than that between C and CA. As a result, the lifetime of the kronian fossil fields was between ~20 min and ~3 hours. These conclusions support previous theoretical estimations within Saturn's magnetosphere (*20*).

The fossil fields could have been removed via diffusion into the collisional ionosphere, convection around the ionosphere into the magnetotail, and reconnection with the IMF. The magnetic shear at locations I and II (111° and 162°, respectively) and the magnetic field variance suggest that reconnection could have occurred during T32. In this scenario (Fig. 4, top panels), Titan could have opened Saturn's magnetopause, and the field reconfiguration could have been similar to that proposed for disconnection events at comets (*21*). Initial real-time modeling supports this interpretation.

However, previous simulations (*20*) indicate that at these altitudes, the plasma density was too low for electrons to be demagnetized. In such a case (Fig. 4, bottom panels), reconnection would not have occurred, and the fossilized fields could have been either diffused into the collisional ionosphere or transported downstream by ambipolar electric fields (*22*) without affecting the magnetic structure of Saturn's magnetopause.

The bow-shock crossings D, E, and F at kronocentric distances of 20.8, 21.0, and 21.4 R_S (Fig. 2, top panel) suggest magnetopause standoff distances around 16 R_S. Hence, it is likely that after T32, Titan remained within Saturn's magnetosheath at least until 23:30, when the fossil fields should have been entirely removed.

References and Notes

1. F. M. Neubauer, D. A. Gurnett, J. D. Scudder, R. E. Hartle, in *Saturn*, T. Gehrels, M. S. Matthews, Eds. (Univ. of Arizona Press, Tucson, AZ, 1984), pp. 760–787.
2. J.-E. Wahlund *et al.*, *Science* **308**, 986 (2005).
3. N. F. Ness, M. H. Acuña, K. W. Behannon, *J. Geophys. Res.* **87**, 1369 (1982).
4. H. Backes *et al.*, *Science* **308**, 992 (2005).
5. K. Szego *et al.*, *Geophys. Res. Lett.* **34**, L24S03 (2007).
6. M. G. Kivelson, *Science* **311**, 1391 (2006).
7. SLT is measured from the noon meridian in the direction of Saturn's rotation.
8. $P_{SW} = \rho v^2$, where ρ and v are the solar wind density and speed, respectively.
9. All times are expressed in UT.
10. M. K. Dougherty *et al.*, *Space Sci. Rev.* **114**, 331 (2004).
11. In the Saturn-centered spherical solar magnetic coordinate system (KSMAG), the polar axis coincides with planet's magnetic axis and λ_{KSMAG} and ϕ_{KSMAG} are, respectively, the magnetic field latitude and azimuth ($\phi_{KSMAG} = 0$ corresponds to the magnetic noon meridian).
12. $R_{MP} = P_{SW}^{-1/4.3}$, where R_{MP} is the magnetopause's standoff distance.
13. C. S. Arridge *et al.*, *J. Geophys. Res.* **111**, A11227 (2006).
14. A. Masters *et al.*, *J. Geophys. Res.* 10.1029/2008JA013276 (2008).
15. D. A. Gurnett *et al.*, *Space Sci. Rev.* **114**, 395 (2004).
16. D. T. Young *et al.*, *Space Sci. Rev.* **114**, 1 (2004).
17. In the Titan-centered spherical ionospheric interaction coordinate system (TIIS), the equatorial plane contains the direction to Saturn (Y_{TIIS}) and that of the nominal corotation flow (X_{TIIS}). λ_{TIIS} and ϕ_{TIIS} are, respectively, the latitude and azimuth (measured from X_{TIIS} toward Y_{TIIS}).
18. H. J. McAndrews *et al.*, *J. Geophys. Res.* **113**, A04210 (2008).
19. R. E. Hartle *et al.*, *Geophys. Res. Lett.* **33**, L08201 (2006).
20. H. Backes, thesis, University of Cologne, Germany (2005).
21. M. B. Niedner, J. C. Brandt, *Astrophys. J.* **223**, 655 (1978).
22. A. J. Coates *et al.*, *Geophys. Res. Lett.* **34**, L24S05 (2007).

23. We thank A. Balogh, T. Horbury, W. S. Kurth, C. Mazelle, S. J. Schwartz, and C. T. Russell for useful discussions, and N. Powell for artwork. C.B. was supported by a Science and Technology Facilities Council Postdoctoral Fellowship.

29 April 2008; accepted 28 July 2008
10.1126/science.1159780

Postseismic Relaxation Along the San Andreas Fault at Parkfield from Continuous Seismological Observations

F. Brenguier,[1,2]* M. Campillo,[2] C. Hadziioannou,[2] N. M. Shapiro,[1] R. M. Nadeau,[3] E. Larose[2]

Seismic velocity changes and nonvolcanic tremor activity in the Parkfield area in California reveal that large earthquakes induce long-term perturbations of crustal properties in the San Andreas fault zone. The 2003 San Simeon and 2004 Parkfield earthquakes both reduced seismic velocities that were measured from correlations of the ambient seismic noise and induced an increased nonvolcanic tremor activity along the San Andreas fault. After the Parkfield earthquake, velocity reduction and nonvolcanic tremor activity remained elevated for more than 3 years and decayed over time, similarly to afterslip derived from GPS (Global Positioning System) measurements. These observations suggest that the seismic velocity changes are related to co-seismic damage in the shallow layers and to deep co-seismic stress change and postseismic stress relaxation within the San Andreas fault zone.

Information about the stress variations in deeper parts of continental faults can be obtained by studying source properties of microearthquakes (*1*). Changes in seismic velocities measured by using repeated natural and active seismic sources can also provide information about rock damage and healing at depth after large earthquakes (*2*, *3*) or about stress changes in seismogenic zones (*4*). The main limitation of these types of measurements, however, is the episodic nature of their seismic sources, which prevents continuous monitoring of crustal properties.

We used continuous measurements of ambient seismic noise to recover continuous variations of seismic velocities within the crust along the San Andreas fault (SAF) near Parkfield, California. With this approach, the cross-correlation function of ambient seismic noise computed between a pair of receivers converges toward the response of Earth between the receivers (the so-called Green's function). Essentially this function represents the seismogram that would be recorded at one of the receivers if a source were acting at the second (*5*, *6*). The

temporal evolution of the crust is then tracked by computing cross-correlation functions at different dates for the same receiver pair and measuring the changes between the correlation functions (*7*–*9*).

To monitor variations in seismic velocity along the SAF at Parkfield, we used more than 5 years of continuous seismic noise data recorded by 13 short-period seismological stations of the Berkeley High Resolution Seismic Network (HRSN) (*10*). These stations are installed in boreholes at depths of 60 to 300 m, thus reducing locally generated noise and effects of temperature variations and precipitation (Fig. 1). We analyzed data from January 2002 to October 2007, spanning the times of two major earthquakes that occurred within a 100-km radius of Parkfield: the moment magnitude (M_w) = 6.5 San Simeon earthquake of 22 December 2003, whose epicenter was located 60 km west of Parkfield, and the M_w = 6.0 Parkfield earthquake of 28 September 2004. For every possible pair combination of stations, we computed the daily cross-correlation of seismic noise by using the procedure of (*11*), yielding 91 × 2140 days = 194,740 cross-correlation and auto-correlation time functions. A reference Green function (RGF) was computed for each station pair by stacking the daily cross-correlations for the entire 2140-day period (*12*). The velocity changes were then determined by measuring time delays between the RGF and 30-day stacks of cross-correlation functions in the frequency range from 0.1 to 0.9 Hz (*9*, *12*, *13*) (Fig. 2B). If the medium experiences a spatially homogeneous relative seismic velocity change, $\Delta v/v$, the relative travel time shift ($\Delta\tau/\tau$) between a perturbed and reference Green function is independent of the lapse time (τ) at which it is measured and $\Delta v/v = -\Delta\tau/\tau$ = constant. Therefore, when computing a local time shift, $\Delta\tau$, between the reference and a chosen cross-correlation function in a short window centered at time τ, we would expect that $\Delta\tau$ should be a linear function of τ. By measuring the slope of the travel time shifts $\Delta\tau$ as a function of time τ, we then estimated the relative time perturbation ($\Delta\tau/\tau$), which is the opposite value of the medium's relative velocity change ($\Delta v/v$). The 30-day stacked correlations shown in Fig. 2A exhibit variations because of the seasonal pattern of the location of noise sources (*14*, *15*). Because these seasonal variations mainly affect the direct waves, we did not make differential time measurements for these waves. We also investigated the accuracy of the station clocks by analyzing the temporal symmetry of the correlation functions (*16*) and correcting for the detected errors (*12*). Lastly, following (*9*), we averaged the measured time shifts for each time τ over all station pairs to increase the measurement accuracy.

After the San Simeon earthquake, the seismic velocity along the SAF at Parkfield decreased by 0.04% (Fig. 3). This is consistent with measurements using active sources and fault guided waves that are associated with other earthquakes (*2*, *3*, *17*). Creepmeter and Global Positioning System (GPS) measurements show that there was no substantial slip detected along the SAF in the Parkfield area after the San Simeon earthquake (*18*). This suggests that the velocity change we detected may be related to co-seismic damage in the shallow layers caused by strong ground shaking (~0.15 g) from this quake. By 7 months after the quake, velocities in the Parkfield area appear to have returned to their pre-earthquake levels.

Kinematic and dynamic rupture inversions as well as GPS and INSAR (Interferometric Synthetic Aperture Radar) measurements showed that the Parkfield mainshock released a maximum stress of 10 Mpa and that the average slip was about 0.5 m (*19*). The Parkfield mainshock was also followed by postseismic afterslip that is still ongoing and broadly distributed between the surface and a depth of 12 km (*20*, *21*). Immediately after the Parkfield earthquake, velocities decreased by 0.08%, and postseismic velocities remained low for almost 3 years (Fig. 3). The long-term decay of the relative velocity perturbation was very similar to the relaxation curve associated with the along-fault displacement deduced from GPS measurements (*21*, *22*). Therefore, our hypothesis is that the evolution of the observed seismic velocity changes after the Parkfield earthquake was governed by the postseismic stress relaxation within deeper parts of the fault zone and the surrounding region.

Observation of nonvolcanic tremors in the vicinity of the Parkfield area supports this hypothesis (Fig. 3). We considered the 30-day averaged rate of tremor activity in the Cholame-Parkfield region computed by using continuous records from the HRSN for the period 2002 through 2007. These tremors are estimated to have occurred between 20- and 40-km depths (*23*), similarly to the episodic tremor and slip phenomena on subduction zones (*24*, *25*). There is clear evidence of triggering of tremor activity by both San-Simeon and Parkfield earthquakes. After the Parkfield earthquake, tremor activity remained elevated and has yet to return to its pre-event level similarly to the seismic velocity changes. This observation supports our hypothesis that both seismic velocity changes and tremor activity after the Parkfield earthquake are related to postseismic stress relaxation and corresponding slow slip. We also propose that the increased nonvolcanic tremor activity after the San Simeon earthquake may be related to slow slip at depth in response to small stress variations induced by the passing of seismic waves from the M_w = 6.5 event (*26*).

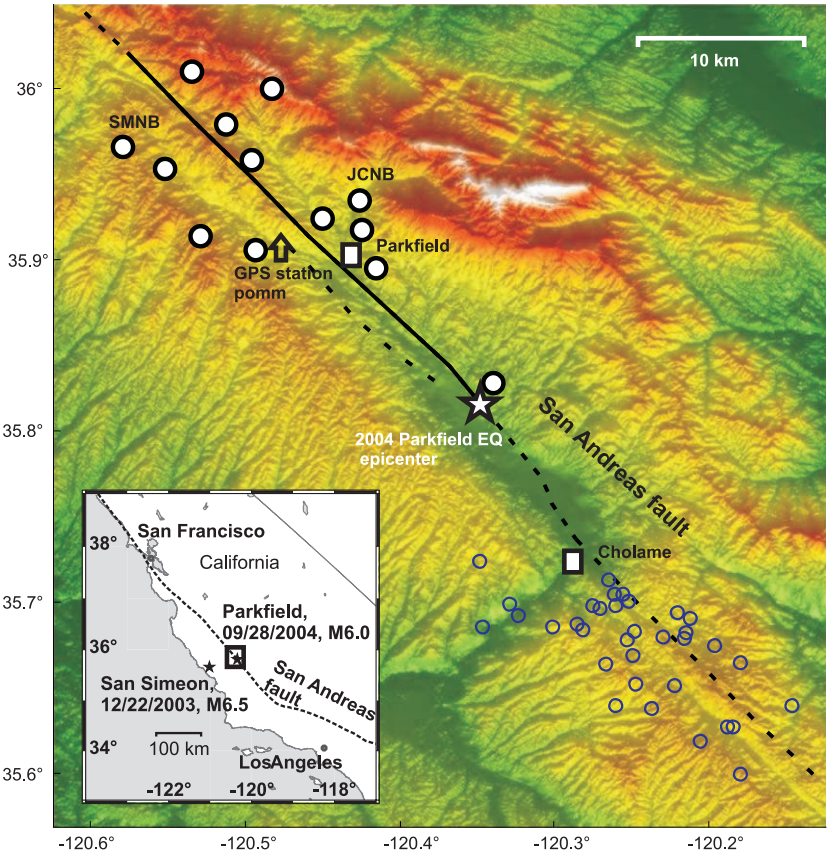

Fig. 1. Location of the HRSN (white and black circles) near Parkfield, California, and location of the 2003 San Simeon and 2004 Parkfield earthquakes. The black solid line indicates the surface projection of the 2004 Parkfield earthquake rupture and afterslip extent. The blue circles indicate the epicenters of nonvolcanic tremors detected by (*23*). The black box on the inset image corresponds to the studied area. The DEM plot was obtained from (*27*, *28*). EQ indicates earthquake.

[1]Sismologie, Institut de Physique du Globe de Paris (IPGP) and CNRS, 4 Place Jussieu, 15252 Paris, France. [2]Laboratoire de Géophysique Interne et Tectonophysique, Université Joseph Fourier and CNRS, 38041 Grenoble, France. [3]Berkeley Seismological Laboratory, University of California Berkeley, 215 McCone Hall, Berkeley, CA 94760, USA.

*To whom correspondence should be addressed. E-mail: fbrengui@ipgp.jussieu.fr

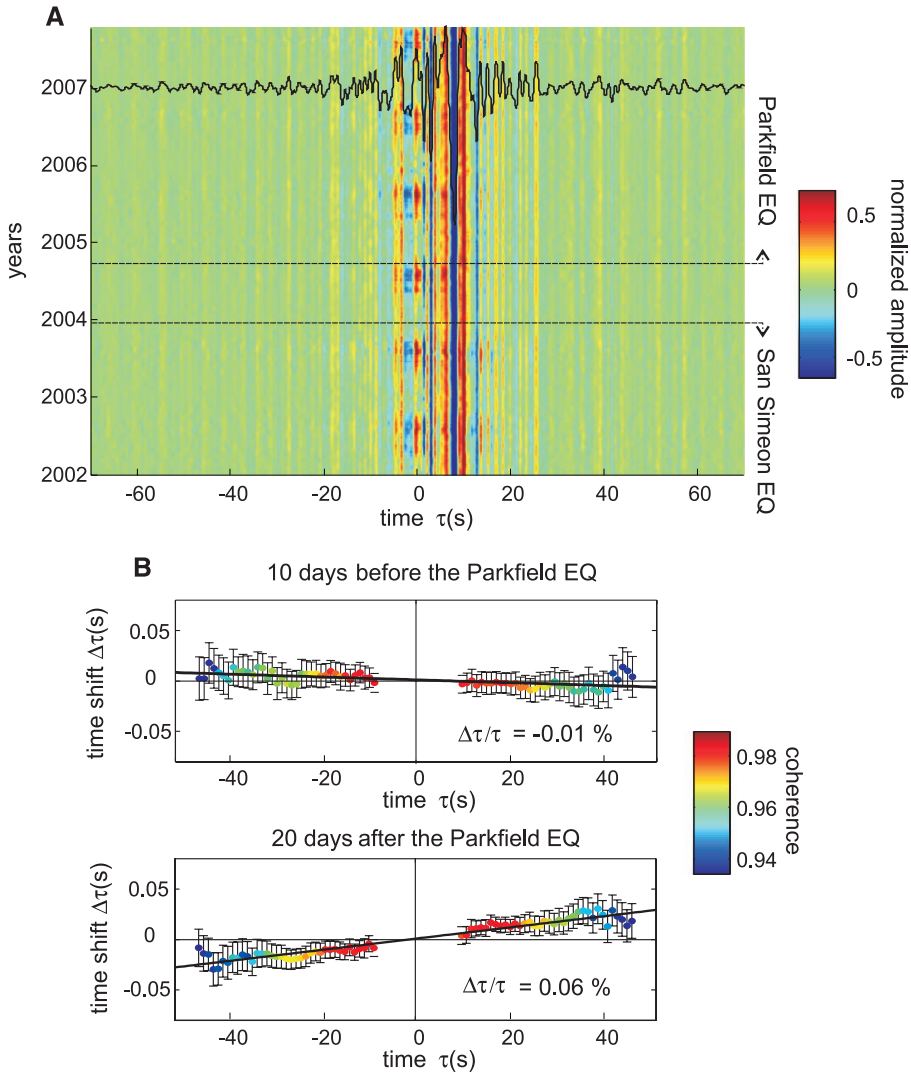

Fig. 2. Relative travel-time change measurements ($\Delta\tau/\tau$). (**A**) Thirty-day stacked cross-correlation functions (CCF) for receiver pair JCNB-SMNB. The black curve represents the reference stacked cross-correlation function. The CCFs are filtered between 0.1 and 0.9 Hz and normalized in amplitude. (**B**) Time shifts averaged over 91 receiver pairs and coherence measured between the reference stacked and 30-day stacked cross-correlation functions (frequency band, 0.1 to 0.9 Hz).

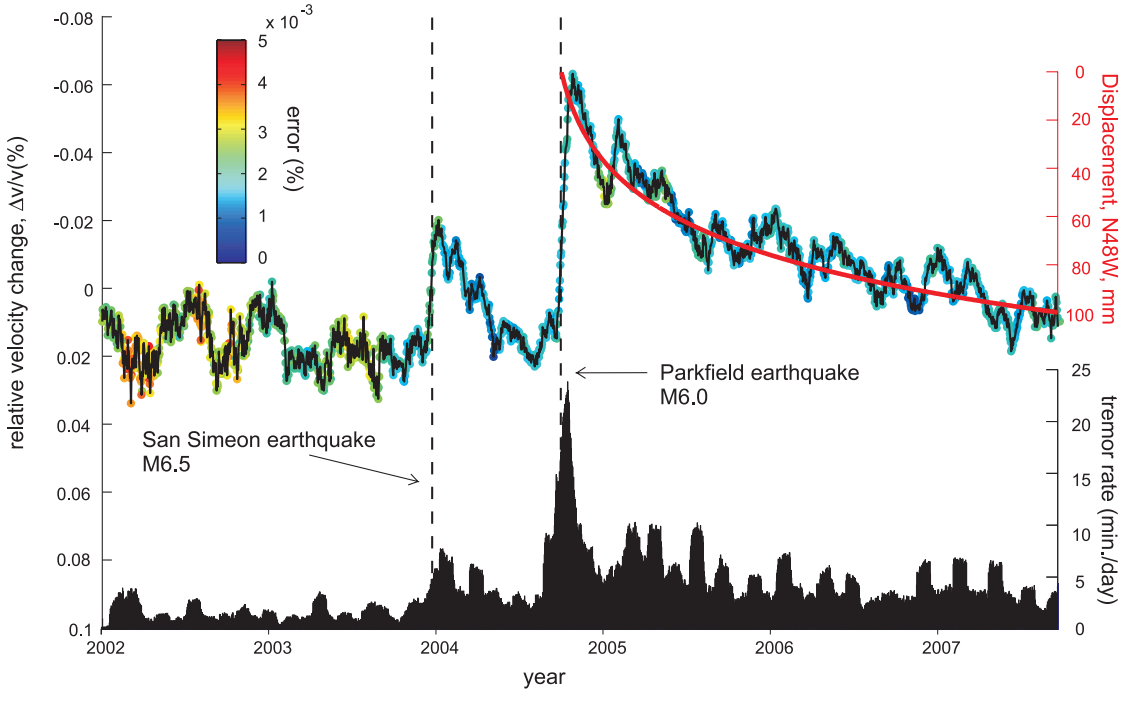

Fig. 3. Seismic velocity changes, surface displacements from GPS, and tremor activity near Parkfield. The red curve represents the postseismic fault-parallel displacements along the San Andreas fault as measured by GPS at station pomm (Fig. 1) (*29*). The tremor rates are averaged over a centered 30-day-length moving time window.

Differences in the evolution of seismic velocities after the San Simeon and the Parkfield earthquakes indicate that two different physical mechanisms may be responsible for the changes in crustal properties: (i) damage of shallow layers and fault zone caused by the strong ground shaking and (ii) co-seismic stress change followed by the postseismic relaxation. These results demonstrate that measuring small velocity perturbations from correlations of seismic noise can be a useful tool for studying the continuous time evolution of the stress regime in the vicinity of seismogenic faults.

References and Notes

1. B. Allmann, P. Shearer, *J. Geophys. Res.* **112**, B04305 (2007).
2. J. E. Vidale, Y. Li, *Nature* **421**, 524 (2003).
3. Y. Li, J. E. Vidale, S. Day, D. Oglesby, E. Cochran, *Bull. Seismol. Soc. Am.* **93**, 854 (2003).
4. F. Niu, P. G. Silver, T. M. Daley, X. Cheng, E. L. Majer, *Nature* **454**, 204 (2008).
5. N. M. Shapiro, M. Campillo, L. Stehly, M. H. Ritzwoller, *Science* **307**, 1615 (2005).
6. M. Campillo, *Pure Appl. Geophys.* **163**, 475 (2006).
7. C. Sens-Schönfelder, U. Wegler, *Geophys. Res. Lett.* **33**, L21302 (2006).
8. U. Wegler, C. Sens-Schönfelder, *Geophys. J. Int.* **168**, 1029 (2007).
9. F. Brenguier *et al.*, *Nat. Geosci.* **1**, 126 (2008).
10. More details concerning the Parkfield HRSN can be found at http://seismo.berkeley.edu/bdsn/hrsn.overview.html.
11. F. Brenguier, N. M. Shapiro, M. Campillo, A. Nercessian, V. Ferrazzini, *Geophys. Res. Lett.* **34**, L02305 (2007).
12. Materials and methods are available as supporting material on *Science* Online.
13. G. Poupinet, W. L. Ellsworth, J. Frechet, *J. Geophys. Res.* **89**, 5719 (1984).
14. L. Stehly, M. Campillo, N. Shapiro, *J. Geophys. Res.* **111**, B10306 (2006).
15. S. Kedar, F. H. Webb, *Science* **307**, 682 (2005).
16. L. Stehly, M. Campillo, N. Shapiro, *Geophys. J. Int.* **171**, 223 (2007).
17. J. L. Rubinstein, G. Beroza, *Geophys. Res. Lett.* **32**, L14313 (2005).
18. More details concerning the U.S. Geological Survey (USGS) deformation network at Parkfield can be found at http://earthquake.usgs.gov/research/parkfield/deform.php.
19. S. Ma, S. Custódio, R. Archuleta, P. Liu, *J. Geophys. Res.* **113**, B02301 (2008).
20. K. M. Johnson, R. Burgmann, K. Larson, *Bull. Seismol. Soc. Am.* **96**, S321 (2006).
21. A. Freed, S. Ali, R. Bürgmann, *Geophys. J. Int.* **169**, 1164 (2007).
22. I. Johanson, E. Fielding, F. Rolandone, R. Burgmann, *Bull. Seismol. Soc. Am.* **96**, S269 (2006).
23. R. M. Nadeau, D. Dolenc, *Science* **307**, 389 (2005); published online 9 December 2004 (10.1126/science.1107142).
24. K. Obara, *Science* **296**, 1679 (2002).
25. G. Rogers, H. Dragert, *Science* **300**, 1942 (2003); published online 8 May 2003 (10.1126/science.1084783).
26. J. Rubinstein *et al.*, *Nature* **448**, 579 (2007).
27. The digital elevation model (DEM) was obtained from the USGS National Map Seamless Server, http://seamless.usgs.gov.
28. J. F. Luis, *Comput. Geosci.* **33**, 31 (2007).
29. More details concerning the USGS GPS network at Parkfield can be found at http://quake.usgs.gov/research/deformation/twocolor/pkf_continuous_gps.html.

30. All of the data used in this study came from the Parkfield HRSN and were collected by the Berkeley Seismological Laboratory (BSL) with support from the USGS under grant 07HQAG0014. We are grateful to the BSL staff. We thank P. Bernard and J. P. Gratier for discussions, O. Coutant for providing us with the doublet analysis code, and G. Moguilny for maintaining the Cohersis cluster. We acknowledge the December 2007 joint BSL/IPGP workshop. This work was supported by Agence Nationale de la Recherche (France) under contracts 05-CATT-010-01 (PRECORSIS) and ANR-06-CEXC-005 (COHERSIS); by NSF under grants EAR-0537641 and EAR-0544730; and by USGS under grant 06HQGR0167. This is Institut de Physique du Globe de Paris (IPGP) contribution no. 2393.

Supporting Online Material

www.sciencemag.org/cgi/content/full/321/5895/1478/DC1
Materials and Methods
Fig. S1

27 May 2008; accepted 17 July 2008
10.1126/science.1160943

Atmospheric Warming and the Amplification of Precipitation Extremes

Richard P. Allan[1]* and Brian J. Soden[2]

Climate models suggest that extreme precipitation events will become more common in an anthropogenically warmed climate. However, observational limitations have hindered a direct evaluation of model-projected changes in extreme precipitation. We used satellite observations and model simulations to examine the response of tropical precipitation events to naturally driven changes in surface temperature and atmospheric moisture content. These observations reveal a distinct link between rainfall extremes and temperature, with heavy rain events increasing during warm periods and decreasing during cold periods. Furthermore, the observed amplification of rainfall extremes is found to be larger than that predicted by models, implying that projections of future changes in rainfall extremes in response to anthropogenic global warming may be underestimated.

Predicting and adapting to changes in the global water cycle expected to result from global warming presents one of the greatest challenges to humanity. Projections of tropical precipitation through this century anticipate increases in moist equatorial regions and indications of drying over the already-arid subtropics (*1*–*6*), changes consistent with theoretical considerations (*7*–*9*). Low-level moisture rises with temperature at about 7%/K, as expected from the Clausius Clapeyron equation (*10*, *11*), fueling comparable rises in heavy precipitation events driven by moisture convergence (*8*). Mean precipitation and evaporation are constrained by the slower rises in atmospheric radiative cooling to the surface (*7*, *12*, *13*). This leads to a decline in precipitation away from the convectively driven regimes that the models achieve through reduced water vapor mass flux and wind stress associated with a weakening of the Walker circulation (*14*). Observational evidence supports the findings that moist regions are becoming wetter and dry regions drier (*3*, *15*, *16*), but the overall response of the models to the current warming trend appears underestimated (*11*, *15*–*17*) and the cause of this discrepancy may affect the fidelity of climate predictions.

Present-day changes in the tropical water cycle are dominated by the periodic warming and moistening associated with El Niño Southern Oscillation (ENSO). Figure 1 shows that warm ENSO events (positive Nino-3 index) are associated with higher column water vapor and precipitation, whereas the reverse is true for cold events. This variability provides a means for testing hypotheses regarding how precipitation responds to a warmer climate. The contrasting mechanisms involved in driving heavy and light precipitation necessitate the examination of daily data (*5*, *18*): We compared daily precipitation from the Special Sensor Microwave Imager (SSM/I) over the tropical oceans (*11*) to multiple Coupled Model Intercomparison Project 3 (CMIP3) models (*19*) forced with present-day sea surface temperature (SST) and with projected greenhouse gas concentrations for the 21st century.

The SSM/I data resolution was degraded to 2.5° by 2.5°, a resolution that is more comparable with climate model grids. Each month of daily precipitation maps was partitioned into 12 bins ranging from the lightest 10% up to the heaviest 1% [supporting online material (SOM) text]. Because climate models struggle to simulate the observed distribution of rainfall intensities (*20*), we calculated changes in precipitation frequency in each bin separately for the satellite data and for each model. Bin boundaries were calculated from 1 year of daily data for the models and the satellite data; the year chosen does not alter the boundary rainfall intensity by more than 10% (table S1). Deseasonalized anomalies in the frequency of precipitation were calculated for each bin. The percentage changes in precipitation frequency, relative to the mean frequency for each bin, were thus calculated for each bin every month.

Figure 2 presents the percentage changes in precipitation frequency in each bin for the SSM/I data and models. These are comparable with results from the SSM/I data for 10 exact 10% bins at the original and the degraded resolutions (fig. S1) and for individual models (fig. S2). There is a coherent variability in observed very heavy precipitation, with higher frequencies associated with warm El Niño events (1988, 1991, 1997–8, and 2002–3) and lower frequencies with cold La Niña events (1989, 1996, and 1999–2000). The model ensemble mean (Fig. 2B) shows qualitative agreement with the satellite data for the heaviest rainfall bins; agreement

[1]Environmental Systems Science Centre, University of Reading, Berkshire RG6 6AL, UK. [2]Rosenstiel School of Marine and Atmospheric Sciences, University of Miami, FL 33149, USA.

*To whom correspondence should be addressed. E-mail: r.p.allan@reading.ac.uk